ELSEVIER

Journal of Organometallic Chemistry 555 (1998) 35–47

Journal of Organometallic Chemistry

Stereochemically non-rigid transition metal complexes of 2,6-bis[1-(phenylimino)ethyl]pyridine (BIP). Part 3. Dynamic NMR studies of *fac*-[PtXMe$_3$(BIP)] (X = Cl, Br, or I). Crystal structure of *fac*-[PtIMe$_3$(BIP)]

Keith G. Orrell [a,*], Anthony G. Osborne [a], Vladimir Šik [a], Mateus Webba da Silva [a], Michael B. Hursthouse [b], David E. Hibbs [b], K.M. Abdul Malik [b], Nikolay G. Vassilev [c]

[a] *Department of Chemistry, University of Exeter, Exeter EX4 4QD, UK*
[b] *Department of Chemistry, University of Wales Cardiff, PO Box 912, Park Place, Cardiff CF1 3TB, UK*
[c] *Institute of Organic Chemistry, Bulgarian Academy of Sciences, Sofia 1113, Bulgaria*

Received 5 September 1997

Abstract

The complexes *fac*-[PtXMe$_3$(BIP)] (X = Cl,Br or I;BIP = 2,6-bis[1-(phenylimino)ethyl]pyridine) have been synthesised and characterised as involving BIP as a bidentate chelate ligand. In solution the metal-bound ligand exists in four conformational forms, namely distal and proximal *E,E and E,Z*-isomers. 2D-EXSY NMR has been used to measure 1,4-metallotropic shifts of the PtXMe$_3$ moiety between equivalent distal *E,E* forms, *E,Z* isomerisation of the pendant imine function and restricted C–C rotation of the pendant arm of the BIP ligand. Activation energies, $\Delta G^{\neq}$ (298.15 K), for all these processes are in the range 67–96 kJ mol^{-1} and are essentially halogen independent. A crystal structure of *fac*-[PtIMe$_3$(BIP)] shows that the pendant imine function is in the *E*-conformation and is rotated at an angle of 80.1° to the plane of the pyridine.

Keywords: Platinum; Bis-imine ligand; Fluxionality; 2D-EXSY NMR

1. Introduction

As part of a comprehensive investigation [1,2] on the fluxional motions of complexes involving 2,6-bis[1-(phenylimino)ethyl]pyridine (BIP), the series of complexes *fac*-[PtXMe$_3$(BIP)] (X = Cl, Br, I) was synthesised. There are strong analogies between the trimethylplatinum(IV) moiety and the rhenium tricarbonyl halide moiety discussed previously [2] as both are isoelectronic, form octahedral complexes with the ancillary ligands in a facial arrangement and are very stable moieties. The methyl groups in the trimethylplatinum(IV) moiety have a greater steric requirement than the carbonyl groups of the rhenium tricarbonyl halide moiety and hence may offer greater impediment to some ligand motions. The NMR characteristics of the trimethylplatinum(IV) moiety provide an excellent medium for the study of fluxional motions and the scalar couplings of ^{195}Pt with surrounding nuclei (as far as four bonds away) are useful structural probes.

2. Results

The complexes *fac*-[PtXMe$_3$(BIP)] (X = Cl, Br, I) were all prepared in a similar manner from the reaction of the ligand with the appropriate trimethylplatinum halide in benzene under conditions of light exclusion.

* Corresponding author.

0022-328X/98/$19.00
PII S0022-328X(97)00690-6

Table 1
Analytical data for the complexes *fac*-[PtXMe$_3$(BIP)] (X = Cl, Br, or I)

Complex	M.p. (°C)	Yield[a] (%)	Infrared[b] (cm^{-1})			Analysis[c] (%)		
			ν(C–H)	ν(Pt–C)	ν(Pt–X)	C	H	N
[PtClMe$_3$(BIP)]	203/6 (dec)	84.3	2966	567	248	48.94	4.79	7.13
			2901	523		(48.50)	(4.67)	(7.04)
			2815	513				
[PtBrMe$_3$(BIP)]	216/9 (dec)	82.7	2975	571	—	45.50	4.46	6.63
			2910	527		(45.28)	(4.46)	(6.21)
			2816	516				
[PtIMe$_3$(BIP)]	224/7 (dec)	89.0	2975	568	—	42.36	4.15	6.17
			2910	526		(42.30)	(4.04)	(5.63)
			2816	505				

[a] Yield quoted relative to monomeric metal containing reactant.
[b] Recorded as CsI discs.
[c] Calculated values in parentheses.

The reaction afforded high yields of air-stable, bright-yellow microcrystalline solids that melt with decomposition between 203 and 227°C when using capillaries exposed to the air. Synthetic and analytical details for the complexes are shown in Table 1 and mass spectral data in Table 2. For all three complexes the ion of highest mass number corresponds to the molecular ion of the compound, $[M]^+$. The most abundant fragment for the chloride and bromide complexes corresponds to a loss of halide plus all three methyl groups, $[M–XMe_3]^+$. However the most stable fragment for the iodide corresponds to a loss of halide alone, $[M–I]^+$. For all cases the observed and calculated isotope patterns are consistent. The IR spectra contain three bands assigned to C–H stretching modes and three due to Pt–C stretching modes. The latter set of absorptions is characteristic of the *fac*-[PtXMe$_3$] moiety [3–5]. There is no general trend for these absorptions in the halide series. The Pt–Cl stretch is only observed for terminal-bound chloride. Other Pt–X (terminal) stretches are expected to occur below 200 cm^{-1}.

2.1. X-ray crystallography

The crystal structure of the iodine derivative, *fac*-[PtIMe$_3$(BIP)], was determined to confirm the proposed stereochemistry. It was found that the compound consists of discrete molecules of *fac*-[PtIMe$_3$(BIP)] held together in the crystal by van der Waals forces only. The structure of a single molecule together with the atom numbering scheme is shown in Fig. 1. Molecular geometry parameters are listed in Table 3. The study confirms the octahedral coordination for the Pt atom with the facial disposition of the three methyl groups. Although the BIP ligand is potentially terdentate, in the present compound it is bonded to Pt in a bidentate manner. The pendant imine function is placed outside the coordination sphere and appears to adopt the *E*-conformation. The Pt–N distances are unequal, with the bond to the pyridyl nitrogen being longer than that to the imine nitrogen [Pt–N(1) 2.243(5) vs. Pt–N(2) 2.152(5) Å]. This is in sharp contrast to the situation where a BIP ligand is bonded to a metal in a terdentate manner; in such cases the shortest metal–nitrogen distance is to the pyridyl nitrogen [6–8]. The changeover in relative metal–nitrogen bond lengths between bidentate and terdentate forms of a ligand is also found in the metal complexes of terpyridine, e.g. [Pd(C$_6$F$_5$)$_2$(terpy)] [9], and may be explained in terms of steric interactions. These values may be compared with the Pt–N distances 2.178(5), 2.190(4) and 2.217(14) Å observed in monomeric [PtClMe$_3$(pydz)] [10] and dimeric [(PtIMe$_3$)$_2$(μ-pydz)] [11], respectively. The Pt–Me distances in the present compound vary from 2.039(6) to 2.067(7) Å, which are comparable with the values 2.038(6)–2.077(7) Å observed in [PtClMe$_3$(pydz)] [10] and only slightly smaller than those 2.051(14)–2.11(2) Å in [(PtIMe$_3$)$_2$(μ-pydz)] [11], these values also follow the trend that the equatorial bonds are somewhat shorter than the axial bond. The Pt–I distance at 2.7970(5) Å is only slightly longer than the value 2.7648(12) Å found in [(PtIMe$_3$)$_2$(μ-pydz)] [11].

Table 2
Mass spectral data[a] for *fac*-[PtXMe$_3$(BIP)] (X = Cl, Br or I) complexes

Complex	*m*/*z*
[PtClMe$_3$(BIP)]	588 $[M]^+$, 553 $[M–Cl]^+$, 523 $[M–ClMe_2]^+$, 508[b] $[M–ClMe_3]^+$
[PtBrMe$_3$(BIP)]	633 $[M]^+$, 553 $[M–Br]^+$, 523 $[M–BrMe_2]^+$, 508[b] $[M–BrMe_3]^+$
[PtIMe$_3$(BIP)]	680 $[M]^+$, 553[b] $[M–I]^+$, 523 $[M–IMe_2]^+$, 508 $[M–IMe_3]^+$

[a] Acquired using the LSIMS technique. The values quoted represent the most abundant ions amongst clusters of isotopic species.
[b] Most abundant of the ions quoted.

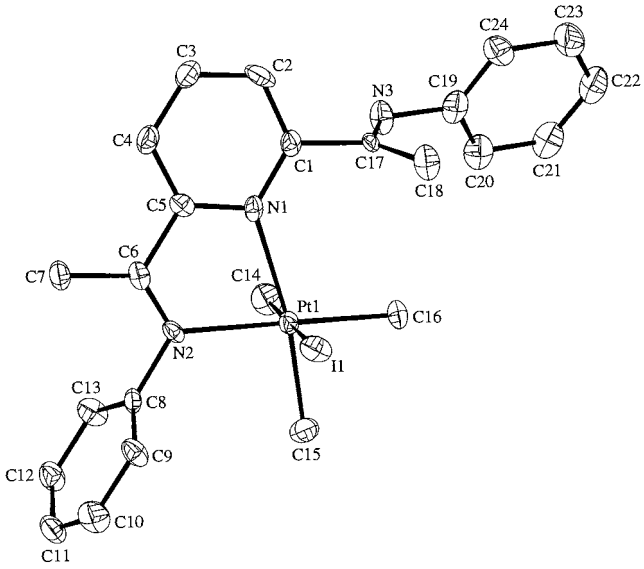

Fig. 1. A view of the crystal structure of *fac*-[$PtIMe_3$(BIP)] showing the atom labelling. Thermal ellipsoids are drawn at 50% probability level.

The octahedron around Pt is as expected somewhat distorted, the main distortion being due to the small BIP 'bite angle' of 74.9(2)°. The I–Pt–Me(eq) angles are obtuse 92.8(2), 94.7(2)°, and I–Pt–N angles are acute 87.56(14), 87.05(13)° which may be explained by the steric requirement of the I and Me ligands. The largest distortion is associated with the N(1)–Pt–C(16) angle, 105.8(2)° which is clearly due to the C(16)···C(18) interaction 3.267(11) Å. The *trans* angles are 171.3(2), 177.5(2) and 178.2(2)°. The pyridine ring is nearly coplanar with the Pt(1)N(1)C(5)C(6)N(2) plane but the phenyl ring C(8)–C(13) is 83.2(2)° rotated out of the latter plane. The imine moiety N(3)C(1)C(17)C(18) makes an angle of 80.1(3)° with the pyridine plane and an angle of 69.1(2)° with the phenyl ring C(19)–C(24). This indicates considerable flexibility of the BIP ligand.

2.2. ^{1}H-NMR studies

^{1}H-NMR spectra for *fac*-[$PtXMe_3$(BIP)] complexes were taken at -10°C in $CDCl_3$. ^{1}H chemical shifts (δ) and coordination shifts ($\Delta\delta$) are recorded in Table 4. Most coordination shifts are positive but significant low frequency coordination shifts occur for the *meta* signals of the pyridyl unit (H_G and H_I). These low frequency shifts are the result of the preferred conformation of the terminal C=N imine bonds relative to the pyridyl ring changing on metal coordination. Opposing trends in the *para* (H_H) versus the *meta* (H_I and H_G) proton signals are characteristic of the distribution of charge in the six-membered heterocycles. With increased electrophilicity of the metal centre the *para* proton is more deshielded and the *meta* protons more shielded.

NOE difference experiments were performed on *fac*-[$PtBrMe_3$(BIP)] in $CDCl_3$ at 30°C. By irradiating the equatorial signal Me_P a positive NOE built up in the signals of the isochronous nuclei of H_O and H_K. This indicates that the nitrogen in the pendant part of the ligand is in a cisoidal orientation in respect to the pyridyl nitrogen, and furthermore, that the relevant phenyl ring is rapidly rotating around the N–C_{ipso} bond. On irradiating signal Me_F a positive NOE built up due to signal H_G but no NOE build up was apparent for signals H_E and H_A. This suggests that the latter protons are almost orthogonal to the chelate plane as the X-ray crystal structure shows (Fig. 1). On irradiating the signal Me_J a positive NOE built up due to signals H_O and H_K. However in contrast to *fac*-

Table 3
Bond lengths (Å) and angles (°) for *fac*-[$PtIMe_3$(BIP)]

Pt(1)–C(15)	2.039(6)	Pt(1)–C(16)	2.051(6)
Pt(1)–C(14)	2.067(7)	Pt(1)–N(2)	2.152(5)
Pt(1)–N(1)	2.243(5)	Pt(1)–I(1)	2.7970(6)
N(1)–C(1)	1.357(8)	N(1)–C(5)	1.361(8)
N(2)–C(6)	1.277(8)	N(2)–C(8)	1.461(8)
N(3)–C(17)	1.291(9)	N(3)–C(19)	1.437(9)
C(1)–C(2)	1.394(9)	C(1)–C(17)	1.511(9)
C(2)–C(3)	1.377(10)	C(3)–C(4)	1.387(10)
C(4)–C(5)	1.389(8)	C(5)–C(6)	1.496(9)
C(6)–C(7)	1.496(9)	C(8)–C(9)	1.360(9)
C(8)–C(13)	1.397(9)	C(9)–C(10)	1.395(10)
C(10)–C(11)	1.358(10)	C(11)–C(12)	1.404(11)
C(12)–C(13)	1.388(10)	C(17)–C(18)	1.483(10)
C(19)–C(24)	1.370(10)	C(19)–C(20)	1.400(9)
C(20)–C(21)	1.389(10)	C(21)–C(22)	1.379(11)
C(22)–C(23)	1.363(10)	C(23)–C(24)	1.408(10)
C(15)–Pt(1)–C(16)	82.9(3)	C(15)–Pt(1)–C(14)	89.5(3)
C(16)–Pt(1)–C(14)	86.5(3)	C(15)–Pt(1)–N(2)	96.4(3)
C(16)–Pt(1)–N(2)	178.2(2)	C(14)–Pt(1)–N(2)	91.8(3)
C(15)–Pt(1)–N(1)	171.3(2)	C(16)–Pt(1)–N(1)	105.8(2)
C(14)–Pt(1)–N(1)	90.0(2)	N(2)–Pt(1)–N(1)	74.9(2)
C(15)–Pt(1)–I(1)	92.8(2)	C(16)–Pt(1)–I(1)	94.7(2)
C(14)–Pt(1)–I(1)	177.5(2)	N(2)–Pt(1)–I(1)	87.05(13)
N(1)–Pt(1)–I(1)	87.56(14)	C(1)–N(1)–C(5)	116.1(5)
C(1)–N(1)–Pt(1)	130.9(4)	C(5)–N(1)–Pt(1)	112.9(4)
C(6)–N(2)–C(8)	118.8(5)	C(6)–N(2)–Pt(1)	119.0(4)
C(8)–N(2)–Pt(1)	122.2(4)	C(17)–N(3)–C(19)	120.9(6)
N(1)–C(1)–C(2)	123.5(6)	N(1)–C(1)–C(17)	119.5(5)
C(2)–C(1)–C(17)	116.9(6)	C(3)–C(2)–C(1)	119.2(6)
C(2)–C(3)–C(4)	118.6(6)	C(3)–C(4)–C(5)	119.3(6)
N(1)–C(5)–C(4)	123.3(6)	N(1)–C(5)–C(6)	116.3(5)
C(4)–C(5)–C(6)	120.4(6)	N(2)–C(6)–C(7)	124.7(6)
N(2)–C(6)–C(5)	116.7(6)	C(7)–C(6)–C(5)	118.7(6)
C(9)–C(8)–C(13)	121.3(6)	C(9)–C(8)–N(2)	120.5(6)
C(13)–C(8)–N(2)	118.2(6)	C(8)–C(9)–C(10)	118.7(6)
C(11)–C(10)–C(9)	121.8(7)	C(10)–C(11)–C(12)	119.3(7)
C(13)–C(12)–C(11)	119.7(7)	C(12)–C(13)–C(8)	119.1(7)
N(3)–C(17)–C(18)	127.6(6)	N(3)–C(17)–C(1)	113.5(6)
C(18)–C(17)–C(1)	118.6(6)	C(24)–C(19)–C(20)	120.5(7)
C(24)–C(19)–N(3)	121.3(6)	C(20)–C(19)–N(3)	118.0(7)
C(21)–C(20)–C(19)	118.6(7)	C(22)–C(21)–C(20)	120.9(7)
C(23)–C(22)–C(21)	120.2(7)	C(22)–C(23)–C(24)	120.0(7)
C(19)–C(24)–C(23)	119.8(7)		

Table 4
[1]H-NMR data[a] for the aromatic region for BIP and the complexes *fac*-[PtXMe$_3$(BIP)] (X = Cl, Br or I) in $CDCl_3$ at −10°C (400.13 MHz)

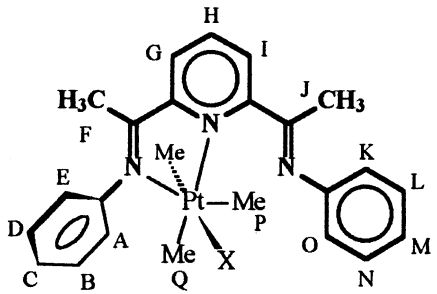

Compound	Me_P $^2J_{PtH}$	Me_Q $^2J_{PtH}$	Me_{axial} $^2J_{PtH}$	A J_{AB} J_{AC} $\Delta\delta$	B J_{BC} J_{BD} $\Delta\delta$	C J_{CD} J_{CE} $\Delta\delta$	D J_{DE} J_{DB} $\Delta\delta$	E J_{ED} J_{EC} $\Delta\delta$	G J_{GH} J_{GI} $\Delta\delta$	H J_{HI} — $\Delta\delta$	I J_{IH} J_{IG} $\Delta\delta$	K J_{KL} J_{KM} $\Delta\delta$	L J_{LM} J_{LN} $\Delta\delta$	M J_{MN} J_{MO} $\Delta\delta$	N J_{NM} J_{NL} $\Delta\delta$	O J_{ON} J_{OM} $\Delta\delta$
				dm 6.88	tm 7.40	tt 7.14	tm 7.40	dm 6.88	d 8.37	t 7.88	d 8.37	dm 6.88	tm 7 40	tt 7.14	tm 7.40	dm 6.88
BIP	—	—	—	8.2	8.2	8.2 1.1	8.2	8.2	7.8	7.8	7.8	8.2	8.2	8.2 1.1	8.2	8.2
				d 7.68	tm 7.47	tt 7.28	tm 7.41	d 6.73	dd 8.10	t 8.15	dd 7.73	dm 6.98	t 7.36	tt 7.14	t 7.36	dm 6.98
Cl	1.32	1.02	0.76	8.4	7.8	7.5	8.1	8.1	7.6	7.6	7.6	8.4	6.5	7.4	6.5	8.4
	71.5	74.1	72.7	—	—	1.0	—	—	1.5	—	1.5	—	—	1.1	—	—
				0.80	0.07	0.14	0.01	−0.15	−0.27	0.27	−0.64	0.10	0.04	0.0	0.04	0.10
				d 7.59	tm 7.48	tt 7.28	tm 7.41	d 6.72	dd 8.15	t 8.08	dd 7.86	dm 6.97	t 7.36	tt 7.13	t 7.36	dm 6.97
Br	1.14	0.83	0.37	7.9	7.6	7.5	7.9	7.9	7.7	7.7	7.7	8.3	7.5	7.4	7.5	8.3
	70.6	73.4	74.3	—	—	1.1	—	—	1.4	—	1.4	—	—	1.1	—	—
				0.71	0.08	0.14	0.01	−0.16	−0.22	0.20	−0.51	0.09	0.04	−0.01	0.04	0.09
				d 7.64	tm 7.48	tt 7.28	tm 7.41	d 6.73	dd 8.10	t 8.15	dd 7.81	dm 6.97	t 7.36	tt 6.97	t 7.36	dm 6.97
I	1.21	0.90	0.53	8.0	7.6	7.5	8.0	8.0	7.6	7.7	7.6	8.5	7.9	8.5	7.9	8.5
	70.9	73.6	74.2	—	—	1.1	—	—	1.4	—	1.4	—	—	1.2	—	—
				0.76	0.08	0.14	0.01	−0.15	−0.27	0.27	−0.56	0.09	0.04	−0.17	0.04	0.09

[a] Chemical shifts (δ) relative to TMS, $\delta = 0$; $\Delta\delta = \delta_{complex} - \delta_{ligand}$; s, singlet; d, doublet; t, triplet; m, multiplet. Scalar couplings in Hertz.

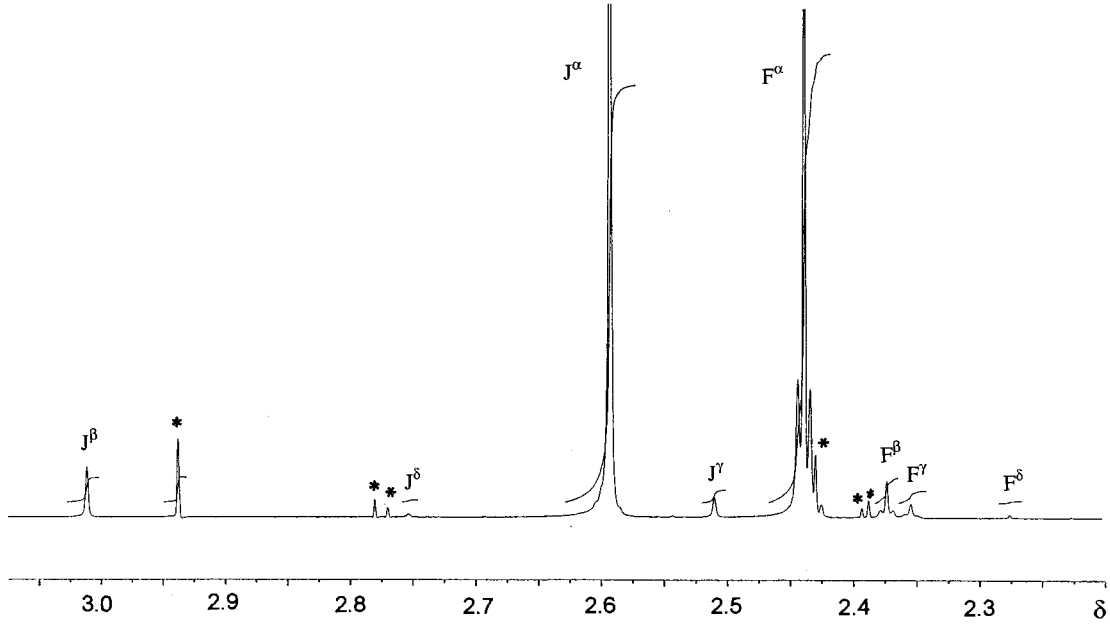

Fig. 2. 400 MHz ^{1}H-NMR spectrum (methyl region) of *fac*-[PtIMe$_3$(BIP)] in $CDCl_3$ at 10°C. See Table 5 for labels. * Other non-fluxional species.

[ReX(CO)$_3$(BIP)] [2] there is no NOE build up due to the *meta* signal H_I of the pyridyl. This suggests that in the structure of *fac*-[PtBrMe$_3$(BIP)] the methyl group Me_J is at a greater average distance from the *meta* proton of the pyridyl ring than in the rhenium complexes [2].

In contrast to the phenyl group of the pendant imine function, the one attached to the metal-bound nitrogen is rotating slowly around the N–C$_{ipso}$ bond and its *ortho* protons show anisochronous signals. The coordination shifts become greater with increased electrophilicity of the metal centre. Signal H_A shows a large positive coordination shift in contrast to signal H_E which shows a small low frequency coordination shift that might be a consequence of H_E falling in the shielding region of the C=N double bond. In the spectra of each of these complexes there is evidence for at least three other species (Fig. 2). Chromatographic separation was tried without success. The elemental analyses were reliable for all three complexes (Table 1). In each coordination complex all minor species were involved in exchange processes with the major species and were assumed to be isomerisation products. The major species was assumed to contain the imine function of the pendant part of the ligand in a distal *E*-conformation (Fig. 3). This was confirmed by the X-ray study on *fac*-[PtIMe$_3$(BIP)]. Steric interactions between the pendant imine function and the metal moiety are likely to be greater than those in the complexes *fac*-[ReX(CO)$_3$(BIP)]. Hence the trimethylplatinum (IV) produces more isomeric species in solution than the rheniumtricarbonyl moiety. These are depicted in Fig. 3 where the labelling follows that used in ref. [2]. The abundance of the major species in these samples increases with an increase in the halide radius (Table 5). However within the minor species the proportions are roughly the same in the series of halides.

2.3. ^{13}C-NMR spectra

The ^{13}C-NMR spectrum of *fac*-[PtIMe$_3$(BIP)] was measured in $CDCl_3$ at 30°C (Table 6). Correlations of the ^{13}C and ^{1}H nuclei were derived from a 2D heteronuclear correlation spectrum. The assignments of the quaternary carbon nuclei are only tentative. The

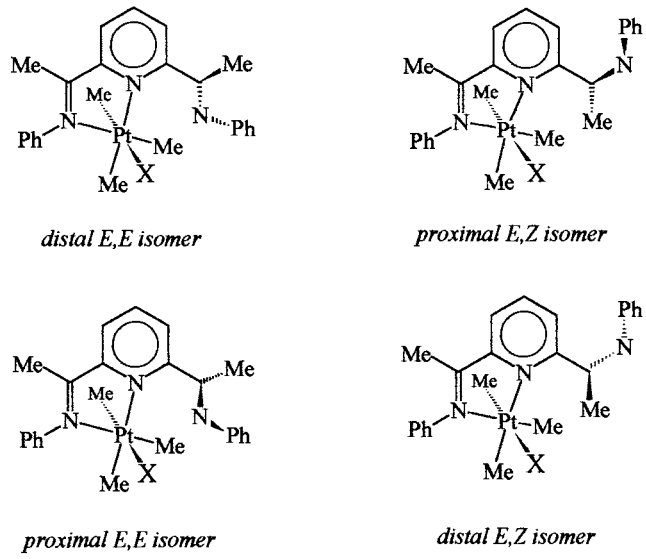

Fig. 3. The proposed solution isomers of the complexes *fac*-[PtXMe$_3$(BIP)] (X = Cl,Br or I).

Table 5
^{1}H-NMR data[a,b] of methyl region for *fac*-[PtXMe$_3$(BIP)] (X = Cl, Br or I) complexes in $CDCl_3$ at 30°C (400.13 MHz)

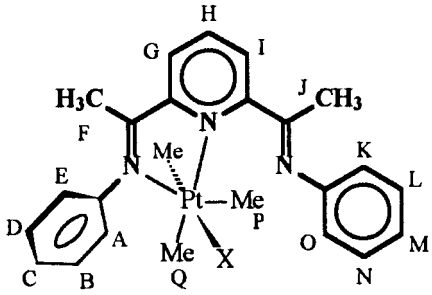

Compound	F^{α} Abundance (%) J_{Pt-H}/Hz	J^{α}	F^{β} Abundance (%)	J^{β}	F^{γ} Abundance (%)	J^{γ}	F^{δ} Abundance (%)	J^{δ}
[PtClMe$_3$(BIP)]	s 2.43 88.19 3.4	s 2.59	2.36 7.69	2.97	2.35 3.57	2.53	2.26 0.55	2.77
[PtBrMe$_3$(BIP)]	s 2.44 89.59 3.6	s 2.59	2.38 6.74	3.00	2.36 3.14	2.52	2.26 0.52	2.77
[PtIMe$_3$(BIP)]	s 2.43 90.96 4.0	s 2.58	2.36 5.69	2.01	2.35 2.84	2.51	2.26 0.51	2.74

[a] Chemical shifts (δ) relative to TMS, $\delta = 0$.
[b] $F^{\alpha}J^{\alpha}$≡distal *E*,*E*; $F^{\beta}J^{\beta}$≡distal *E*,*Z*; $F^{\gamma}J^{\gamma}$≡proximal *E*,*Z*; $F^{\delta}J^{\delta}$≡proximal *E*,*E* (see Fig. 3).

Table 6
^{13}C-NMR data[a] for *fac*-[PtIMe$_3$(BIP)] in $CDCl_3$ at 30°C (100.62 MHz)

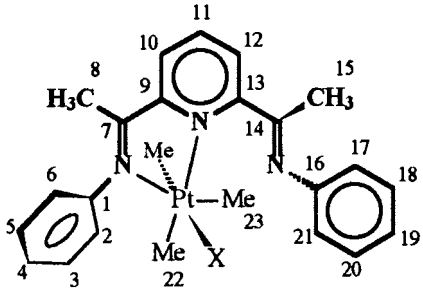

1[b] J_{Pt-C}	2	3	4	5	6	7[b] J_{Pt-C}	8	9[b]	10	11	12
145.88 12.6	123.29	129.60	127.03	128.90	120.32	162.61 12.7	20.47 7.3	155.62 9.0	127.25	139.39	128.25

13[b] J_{Pt-C}	14[b]	15	16[b]	17	18	19	20	21	22 J_{Pt-C}	23 J_{Pt-C}	Pt–Me$_{ax}$ J_{Pt-C}
148.75 5.4	171.99	22.27	168.16	119.98	129.04	124.65	129.04	119.98	−7.62 650.3	−0.61 687.8	7.76 685.4

[a] Chemical shifts (δ) relative to TMS, $\delta = 0$. Scalar couplings in Hertz.
[b] Tentative assignments.

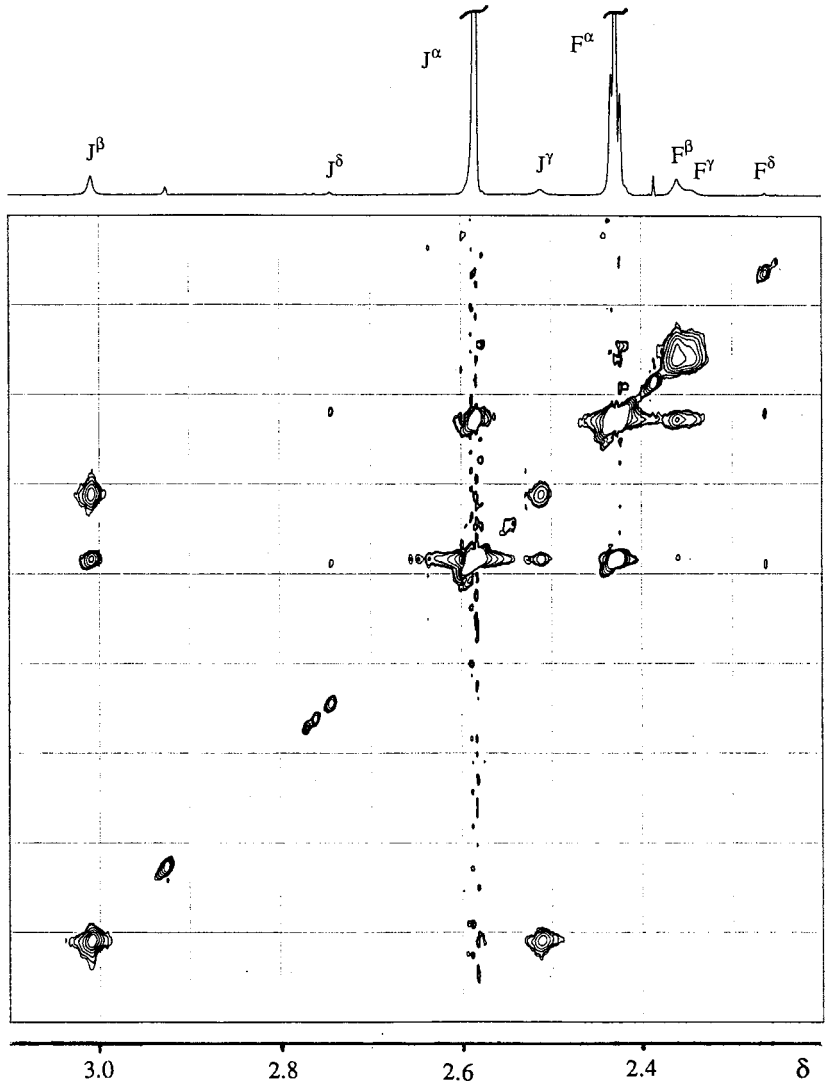

Fig. 4. 400 MHz ^{1}H-NMR 2D-EXSY spectrum of *fac*-[PtIMe$_3$(BIP)] in $CDCl_3$ at 30°C. Mixing time $\tau_m = 1.5$ s.

signals C_1, C_7, C_9, and C_{13} were assigned according to the magnitude of the scalar coupling J_{Pt-C} and the probable effect of the electrophilicity of the metal centre. The distinctions between C_1/C_7 and C_{14}/C_{16} are rather speculative. The coupling associated with signal Me_{22} is much smaller than for other equatorial and axial signals, reflecting the magnitude of the *trans* influence of the pyridyl unit.

2.4. Dynamic NMR studies

A ^{1}H-NMR 1D variable temperature study was carried out to establish the fluxional nature of the various isomers. For all three complexes the spectra showed that the major and the minor species underwent exchange to produce, at the higher temperatures, a spectrum representative of a single rapidly exchanging species. In order to identify the different fluxional motions the 2D-EXSY spectrum of the methyl region of *fac*-[PtIMe$_3$(BIP)] was measured at 30°C (Fig. 4). The most abundant species (distal *E*,*E*) is represented by its methyl signals $F^{\alpha}J^{\alpha}$. Of the minor species, the most populous (distal *E*,*Z*) is represented by its methyl signals $F^{\beta}J^{\beta}$, the next most populous, attributed to the proximal *E*,*Z*, is represented by signals $F^{\gamma}J^{\gamma}$ and the least populous species (proximal *E*,*E*) by signals $F^{\delta}J^{\delta}$.

All the exchange processes identified are summarised in Fig. 5. Cross-peak signals identified the exchanges $F^{\alpha} \rightleftharpoons J^{\alpha}$, $F^{\alpha} \rightleftharpoons F^{\beta}$ (and $J^{\alpha} \rightleftharpoons J^{\beta}$), $F^{\gamma} \rightleftharpoons F^{\delta}$ (and $J^{\gamma} \rightleftharpoons J^{\delta}$), $F^{\alpha} \rightleftharpoons F^{\delta}$ (and $J^{\alpha} \rightleftharpoons J^{\delta}$), and $F^{\beta} \rightleftharpoons F^{\gamma}$ (and $J^{\beta} \rightleftharpoons J^{\gamma}$). The exchange $F^{\alpha} \rightleftharpoons J^{\alpha}$ represents the 1,4-metallotropic shift in the distal *E*,*E* species. There is no metallotropic shift for any other species. The exchanges $F^{\alpha} \rightleftharpoons F^{\beta}$ and $F^{\gamma} \rightleftharpoons J^{\delta}$ correspond to the imine *E*,*Z* isomerisation process of the pendant part of the BIP ligand. Finally, the exchanges $F^{\alpha} \rightleftharpoons F^{\delta}$ and $F^{\beta} \rightleftharpoons F^{\gamma}$ correspond to the restricted rotation of the C–C bond of the pendant part of the BIP ligand.

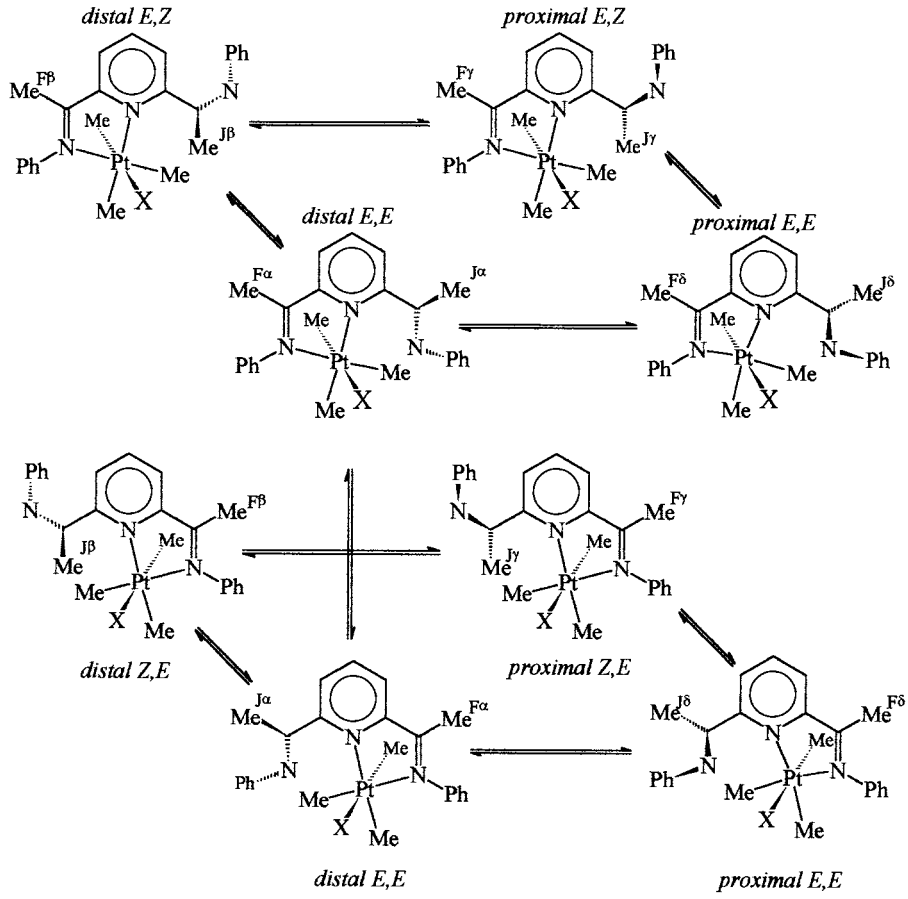

Fig. 5. General exchange scheme for fluxional motions in the complexes *fac*-[$PtXMe_3$(BIP)] (X = Cl,Br or I) showing the nine exchange pathways (four distinct types).

2.5. Kinetic studies

The total spin problem for the exchange processes involves an eight site exchange (Fig. 5). Intensity data of 2D-EXSY signals taken in the temperature range 20–50°C were used to calculate rate data. However the results were not reliable for the C–C restricted rotation processes between the proximal *E,Z* and distal *E,Z* forms, since in this temperature range the diagonal and cross peak signals for the exchange $F^{\beta} \rightleftharpoons F^{\gamma}$ were too broad for accurate measurements. Therefore, 2D-EXSY spectra were measured at a lower temperature range (see later) to derive rate constants for this latter process.

2.5.1. Temperature range 20–50°C

2D-EXSY spectra were measured for the temperature range 20–50°C for complexes *fac*-[$PtXMe_3$(BIP)]. Because the exchange $F^{\beta} \rightleftharpoons F^{\gamma}$ (the C–C restricted rotation processes between proximal *E,Z* and distal *E,Z*) was separated from the total spin problem the latter was formulated as a six-site exchange for this temperature range. The 2D-EXSY signals were converted into a 6×6 intensity matrix **I** by integrating the area under each peak. The method of handling data for the intensity matrix followed the treatment previously described [2]. The rate constants may be read directly from the off-diagonal elements of the calculated matrix **L**. Choice of τ_m values and treatment of errors followed the literature [12].

2.5.2. Temperature range −10 to 20°C

2D-EXSY spectra were performed in $CDCl_3$ in the temperature range −10 to 20°C for these complexes. The aim was to measure the rates of C–C restricted rotation of the pendant arm of the ligand in the minor species, i.e. the exchange distal *E,Z* ⇌ proximal *E,Z* ($F^{\beta} \rightleftharpoons F^{\gamma}$, $J^{\beta} \rightleftharpoons J^{\gamma}$), Fig. 5.

The D2DNMR program [12] was applied to this two-site exchange problem using the diagonal and cross-peaks of the $J^{\beta} \rightleftharpoons J^{\gamma}$ exchange. The 2D-EXSY spectrum of *fac*-[$PtBrMe_3$(BIP)] measured at 10°C with mixing time 1.0 s is shown in Fig. 6.

2.5.3. The mechanisms of fluxional processes

Three different fluxional motions were observed for complexes *fac*-[$PtXMe_3$(BIP)], namely (i) the 1,4-metallotropic shift, (ii) the *E,Z*-diastereoisomerisation of the

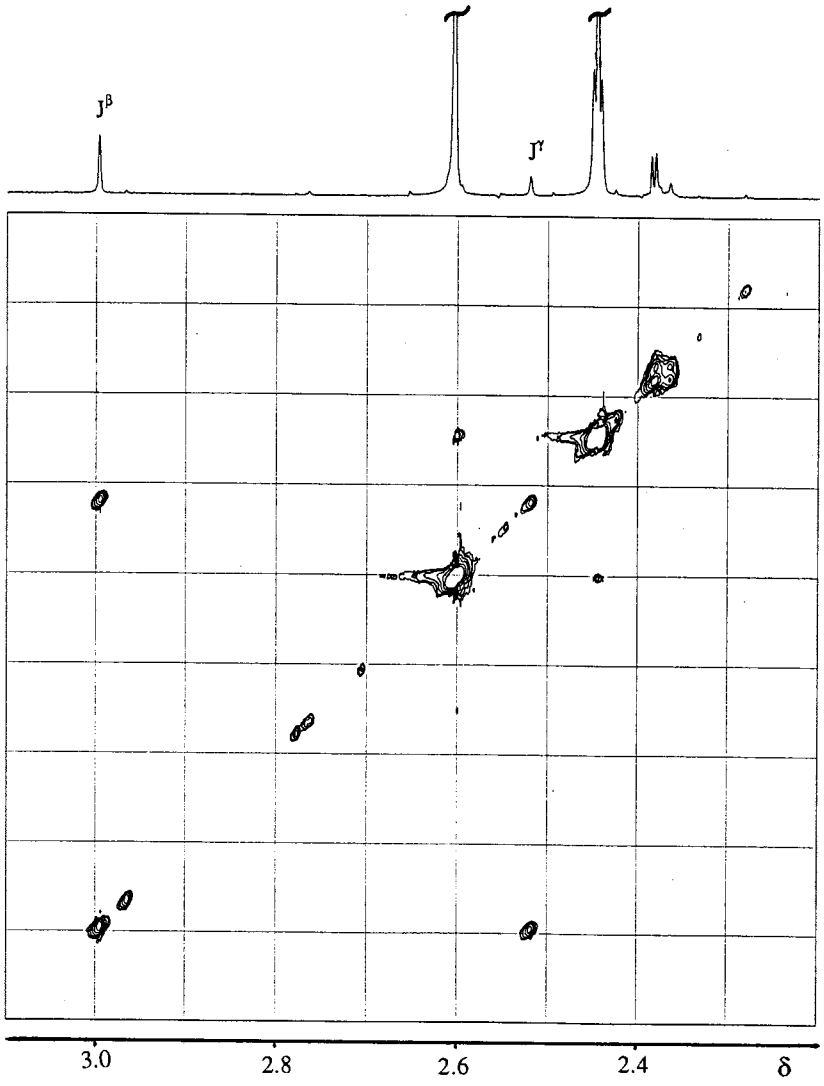

Fig. 6. 400 MHz ^{1}H-NMR 2D-EXSY spectrum of *fac*-[PtBrMe$_3$(BIP)] in $CDCl_3$ at 10°C. Mixing time $\tau_m = 1.0$ s.

pendant imine function, and (iii) the C–C restricted rotation of the pendant part of the BIP ligand. Metal commutation was only observed for the distal *E*,*E*-isomer.^{1}H-NMR spectra of the Pt–Me region of *fac*-[PtIMe$_3$(BIP)] in $(CDCl_2)_2$ in the temperature range 30–130°C were recorded. In the temperature range 30–80°C the equatorial signals broadened while the axial signal remained sharp (Fig. 7). The exchange of the equatorial methyl groups, with no axial group exchange, is a sign that the mechanism proceeds via the 'tick-tock' twist resulting from the ligand trying but failing to adopt terdentate bonding. The tick-tock twist involves a seven coordinate platinum(IV) intermediate (Fig. 8). On further warming, the two equatorial Pt–Me signals and the axial Pt–Me signal start exchanging. Such an exchange or scrambling of Pt–Me environments is a well known feature of *fac*-[PtXMe$_3$(L–L)] compounds [13]. *E*,*Z*-diastereoisomerisation in the pendant imine bond can proceed through a 180° rotation about the C=N double bond, or through an inversion of the nitrogen. In the case of *fac*-[PtXMe$_3$(BIP)] it is not possible to exclude either mechanism. However, on the basis of previous studies [1,14] the favoured mechanism is a nitrogen inversion process.

3. Discussion

Activation energy data were calculated from the derived rate constants from a least-squares fit of the Eyring plots, Table 7. The entropies of activation have magnitudes which cluster around zero, as expected for purely intramolecular rearrangements, but have rather large associated uncertainties. The free energy of activation for all fluxional motions seems to be independent of the electrophilicity of the metal centre. In general the $\Delta G^{\neq}$ values for the three processes, metal commutation, distal *E*,*Z* $\rightleftharpoons$ distal *E*,*E* isomerisation and C–C

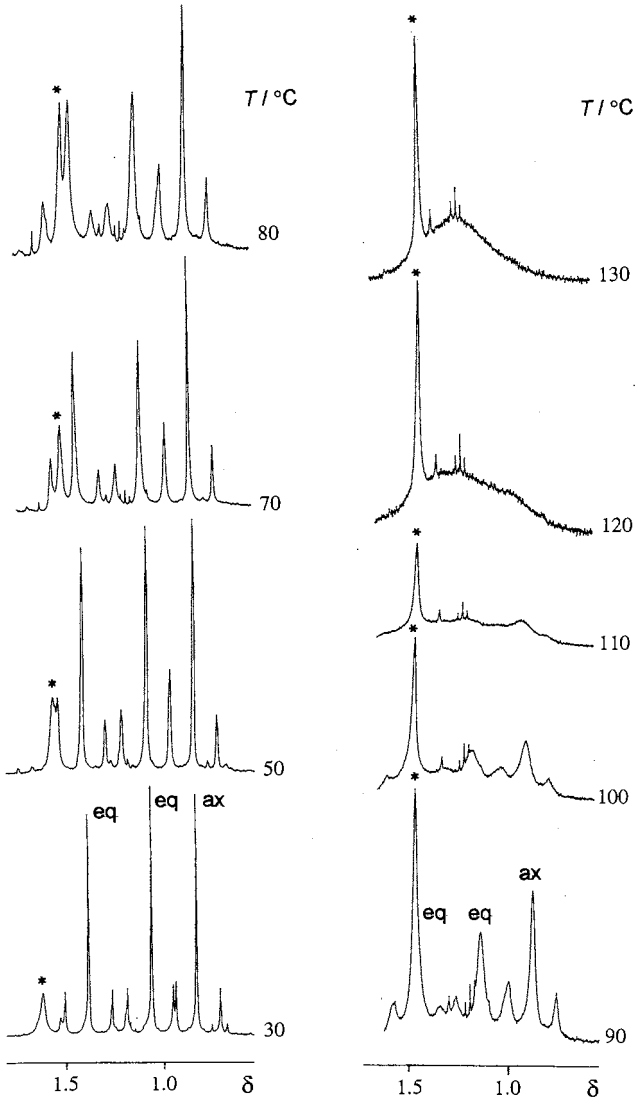

Fig. 7. 300 MHz ^{1}H-NMR spectra (platinum methyl region) of *fac*-[PtIMe$_3$(BIP)] in $(CDCl_2)_2$ in the temperature range 30–130°C, showing the 1,4-metallotropic shift and platinum–methyl scrambling. * An impurity.

restricted rotation proximal *E,E* ⇌ distal *E,E* do not differ greatly in magnitude. However, these values are ca. 10 kJ mol^{-1} greater than the magnitude of $\Delta G^{\neq}$ for the C–C restricted rotation of the *E,Z* rotamers.

This work, together with other parts of this series [1,2], has demonstrated the power of 1D and 2D-NMR techniques for studying the complex internal dynamics of metal complexes of BIP ligands. Rates and activation energies of 1,4-metallotropic shifts, C–C restricted rotation processes and imine isomerisation processes were independently measured despite their similarity in magnitudes.

A fourth process, namely restricted rotation of the phenyl ring on the coordinated imine function was also examined in the present Pt(IV) complexes by a variable temperature ^{13}C-NMR study of the *ortho* carbons of the ring. Spectra recorded in the range 303–403 K revealed a band coalescence effect.

4. Experimental

4.1. Physical measurements

Elemental analyses were carried out by Butterworth Laboratories (Teddington, Middlesex, London). Melting points were recorded open to air on a Gallenkamp melting point apparatus and are uncorrected. Mass spectra were recorded on a Kratos Profile HV-3 spectrometer operating in liquid secondary ion mass spectrometry (LSIMS) mode using a 3-nitro-benzyl alcohol matrix. Infrared spectra were recorded in $CHCl_3$ solutions using matched CaF_2 solution cells on a Perkin-Elmer 881 spectrometer. NMR spectra were recorded on a Bruker DRX400 instrument with ^{1}H recorded at 400.13 and ^{13}C at 100.61 MHz. ^{1}H and ^{13}C{^{1}H} chemical shifts are quoted relative to Me_4Si (TMS). A standard B-VT 2000 variable temperature unit was used to control the probe temperature, the calibration of this unit being checked periodically against a Comark digital thermometer. The temperatures are considered to be accurate to ±1°C. ^{1}H–^{13}C correlation spectra and COSY spectra were obtained with the Bruker automation programs INVBTP and COSY45. 2D-EXSY spectra were obtained with the Bruker automation program NOESYTP. The initial delay time was typically 2.00 s, the evolution time was initially 3×10^{-6} s and the mixing time was varied according to the experimental temperature.

Kinetic data were derived either from band shape analysis of ^{1}H-NMR spectra using the iterative DNMR5 program [15] for the simulation of band

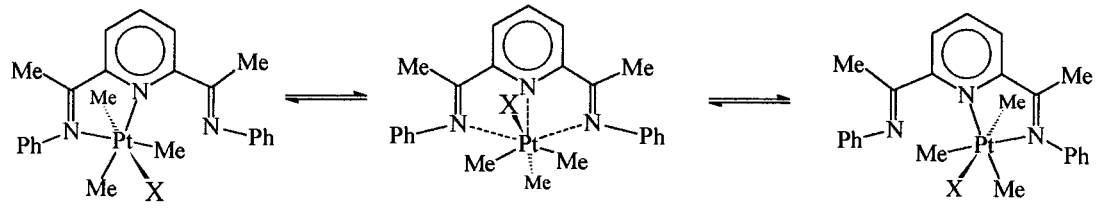

Fig. 8. Proposed mechanism of the 1,4-metallotropic shift.

Table 7
Activation parameters for fluxional processes in complexes *fac*-[PtXMe$_3$(BIP)] (X = Cl, Br, I)

Compound	Process	*k*	$\Delta H^{\neq}$ (kJ mol^{-1})	$\Delta S^{\neq}$ (J mol^{-1} K^{-1})	$\Delta G^{\neq}$ (kJ mol^{-1})[e]
[PtClMe$_3$(BIP)]	[a]		79.68 ± 0.35	1.8 ± 1.1	79.14 ± 0.02
	[b]	f	73.44 ± 2.23	13.8 ± 8.1	69.32 ± 0.19
		r	73.45 ± 2.23	20.9 ± 8.1	67.22 ± 0.19
	[c]	f	84.34 ± 1.82	10.6 ± 5.8	81.19 ± 0.10
		r	91.38 ± 4.87	−7.9 ± 15.2	93.73 ± 0.34
	[d]	f	85.89 ± 6.72	17.1 ± 21.3	80.79 ± 0.36
		r	87.89 ± 1.77	2.0 ± 5.6	87.30 ± 0.10
[PtBrMe$_3$(BIP)]	[a]		81.88 ± 0.69	7.3 ± 2.2	79.69 ± 0.03
	[b]	f	64.48 ± 2.31	−18.8 ± 8.3	70.08 ± 0.17
		r	62.07 ± 2.62	−21.5 ± 9.4	68.49 ± 0.19
	[c]	f	87.24 ± 2.42	21.3 ± 7.7	80.90 ± 0.11
		r	86.92 ± 8.32	−23.2 ± 26.0	93.84 ± 0.58
	[d]	f	74.88 ± 7.20	−18.2 ± 23.1	80.31 ± 0.31
		r	88.47 ± 2.27	3.9 ± 7.3	87.31 ± 0.11
[PtIMe$_3$(BIP)]	[a]		83.64 ± 0.29	12.6 ± 0.9	79.88 ± 0.01
	[b]	f	67.40 ± 0.48	−8.7 ± 1.7	70.01 ± 0.03
		r	67.40 ± 0.48	−3.6 ± 1.7	68.48 ± 0.03
	[c]	f	83.80 ± 0.88	13.0 ± 2.9	79.93 ± 0.03
		r	120.75 ± 9.97	82.4 ± 31.4	96.17 ± 0.62
	[d]	f	78.98 ± 9.10	−6.0 ± 29.4	80.76 ± 0.33
		r	84.42 ± 0.65	−7.9 ± 2.1	86.77 ± 0.02

f, forward and r, reverse processes.
[a] 1,4-Metallotropic shift; [b] C–C restricted rotation distal *E,Z* ⇌ proximal *E,Z*; [c] distal *E,Z* ⇌ distal *E,E* isomerisation; [d] C–C restricted rotation proximal *E,E* ⇌ distal *E,E*; [e] Measured at 298.15 K.

shapes, or from 2D-EXSY spectra using the standard D2DNMR [12] program. Activation parameters were calculated from a least-squares fit of the Eyring plots. Quoted errors are standard deviations based on the uncertainties in the rate constants only.

4.2. Materials

Previously described methods were used to prepare the complexes [PtXMe$_4$] (X = Cl [16], Br and I [17]). The ligand BIP was prepared by condensation of 2,6-diacetylpyridine with aniline in benzene [18].

All preparations were performed by standard Schlenk techniques [19] under purified nitrogen using freshly distilled dried and degassed solvents. The complexes *fac*-[PtXMe$_3$(BIP)] were all prepared in an analogous manner. The preparation of *fac*-[PtIMe$_3$(BIP)] is given as a representative example.

4.2.1. *fac*-[PtIMe$_3$(BIP)]

The complex [PtIMe$_3$]$_4$ (0.10 g, 0.27 mmol, based on monomeric unit) and BIP (0.094 g, 0.3 mmol) were heated under reflux in benzene (25 cm^3) for 7 h. The solvent was subsequently evaporated under reduced pressure and the bright yellow powder was washed with diethylether (2 × 20 cm^3). It was then dried at ca. 50°C for 5 h. Yield 0.165 g, 89.0%.

4.2.2. Crystal structure determination of *fac*-[PtIMe$_3$(BIP)]

Yellow crystals of *fac*-[PtIMe$_3$(BIP)] suitable for X-ray work were obtained by recrystallisation of the crude material from a benzene/hexane mixture.

The unit cell parameters and intensity data were measured at 150 K using a Delft Instruments FAST TV area detector diffractometer positioned at the window of a rotating anode generator using Mo–K$_\alpha$ radiation (λ = 0.71069 Å) by following procedures described elsewhere [20]. The data were corrected for Lorentz and polarisation factors and also for absorption effects [21]. The structure was solved by Patterson methods (SHELXS-86) [22] and difference synthesis and refined on F^2 by full matrix least squares (SHELXL-93) [23] using all unique data. All non hydrogen atoms were anisotropic. The hydrogen atoms were included in calculated positions (riding model) with $U(\text{iso}) = n \times U(\text{eq})$ of the parent atom (n = 1.2 for CH and CH$_2$, 1.5 for CH$_3$). Final R (on F) and wR (on F^2) values were 0.0423 and 0.0954, respectively, for all 2622 data and 267 parameters. The corresponding R values for 3334

data with $I > 2\sigma(I)$ were 0.0393 and 0.0946, respectively. The residual electron density in the final difference map did not indicate any feature of stereochemical significance. Molecular geometry parameters are given in Table 3. The crystal data, details of data collection and structure refinement parameters, and atom coordinates are given in Tables 8 and 9. Anisotropic displacement coefficients, hydrogen atom parameters and structure factor tables have been deposited at the Cambridge Crystallographic Data Centre. Calculations were performed on a Pentium 200 MHz personal computer. Sources of scattering factors were as in ref. [23].

Acknowledgements

We are most grateful to the Ministry of Petroleum (Angola) for financial support (to Mateus Webba da Silva).

Table 8
Crystal data, details of data collection and structure refinement parameters for *fac*-[PtIMe$_3$(BIP)]

Empirical formula	$C_{24}H_{28}IN_3Pt$
Formula weight	680.48
Temperature (K)	150(2)
Wavelength (Å)	0.71069
Crystal system	Monoclinic
Space group	$P2_1/c$
Unit cell dimensions	
a (Å)	13.223(2)
b (Å)	10.4810(10)
c (Å)	17.812(2)
β (°)	106.620(9)
Volume (Å)^3	2365.4(5)
Z	4
Density (calculated) (g cm^{-3})	1.911
Absorption coefficient (mm^{-1})	7.251
F(000)	1296
Crystal size (mm)	$0.25 \times 0.22 \times 0.18$
Theta range for data collection (°)	2.28–25.03
Absorption correction factors	0.887–1.023
Index ranges	$-15 < h < 14$, $-7 < k < 12$, $-20 < l < 20$
Reflections collected	9899
Independent reflections	3622 [R(int) = 0.0561]
Refinement method	Full-matrix least-squares on F^2
Data/restraints/parameters	3622/0/267
Goodness-of-fit on F^2	1.080
R indices[a] (all data)	$R_1 = 0.0423$, $wR_2 = 0.0954$
R indices (data with $I > 2\sigma(I)$)	$R_1 = 0.0393$, $wR_2 = 0.946$
Largest difference peak and hole (eÅ^{-3})	4.389 and −1.266

[a] $R_1 = \Sigma(\Delta F)/\Sigma(F_o)$;
$wR_2 = [\Sigma\{(w\Delta F^2)^2\}/\Sigma\{w(F_o^2)^2\}]^{1/2}$;
$w = 1/[\sigma^2(F_o^2) + (0.0596P)^2]$, where $P = [\max(F_o^2) + 2F_c^2]/3$.

Table 9
Atomic coordinates ($\times 10^4$) and equivalent isotropic displacement parameters (Å$^2 \times 10^3$) for *fac*-[PtIMe$_3$(BIP)]

Atom	x	y	z	U(eq)[a]
Pt(1)	2327.8(2)	1267.1(2)	929.8(1)	18(1)
I(1)	4309.7(4)	1749.6(5)	720.1(2)	27(1)
N(1)	3106(4)	1365(5)	2225(3)	16(1)
N(2)	2879(4)	−640(5)	1263(3)	17(1)
N(3)	1832(4)	3859(5)	2597(4)	24(1)
C(1)	3173(5)	2333(6)	2742(3)	19(1)
C(2)	3680(6)	2224(7)	3542(4)	31(2)
C(3)	4143(6)	1081(7)	3833(4)	30(2)
C(4)	4075(5)	69(7)	3319(4)	25(2)
C(5)	3550(5)	238(6)	2530(3)	17(1)
C(6)	3418(5)	−854(6)	1970(4)	17(1)
C(7)	3900(5)	−2113(6)	2270(4)	26(2)
C(8)	2676(5)	−1694(6)	703(4)	19(1)
C(9)	3309(5)	−1883(6)	231(4)	23(2)
C(10)	3104(6)	−2919(7)	−282(4)	31(2)
C(11)	2288(6)	−3730(6)	−326(4)	29(2)
C(12)	1628(6)	−3520(7)	154(4)	28(2)
C(13)	1819(5)	−2494(7)	668(4)	25(2)
C(14)	895(6)	896(8)	1136(4)	32(2)
C(15)	1663(6)	888(7)	−230(4)	31(2)
C(16)	1754(6)	3065(6)	605(4)	31(2)
C(17)	2714(5)	3623(6)	2450(4)	19(2)
C(18)	3347(5)	4502(7)	2112(4)	28(2)
C(19)	1331(5)	5083(7)	2422(4)	26(2)
C(20)	366(5)	5146(7)	1835(4)	31(2)
C(21)	−150(6)	6313(7)	1684(5)	33(2)
C(22)	272(6)	7388(8)	2104(4)	35(2)
C(23)	1193(6)	7312(8)	2692(4)	37(2)
C(24)	1733(6)	6141(7)	2856(4)	28(2)

[a] U(eq) is defined as one third of the trace of the orthogonalised U_{ij} tensor.

References

[1] K.G. Orrell, A.G. Osborne, V. Šik, M. Webba da Silva, J. Organomet. Chem. 530 (1997) 235.
[2] K.G. Orrell, A.G. Osborne, V. Šik, et al., J. Organomet. Chem. 538 (1997) 171.
[3] D.E. Clegg, J.R. Hall, J. Organomet. Chem. 22 (1970) 491.
[4] P.A. Bulliner, V.A. Maroni, T.G. Spiro, Inorg. Chem. 9 (1970) 1887.
[5] D.E. Clegg, J.R. Hall, G.A. Swile, J. Organomet. Chem. 38 (1972) 403.
[6] G.J. Stor, M. van der Vis, D.J. Stufkins, A. Oskam, J Fraanje, K. Goubitz, J. Organomet. Chem. 482 (1994) 15.
[7] E.C. Alyea, G. Ferguson, R.J. Restivo, Inorg. Chem. 14 (1975) 2491.
[8] D.A. Edwards, M.F. Mahon, W.R. Martin, K.C. Molloy, P.E. Fanwick, R.A. Walton, J. Chem. Soc. Dalton Trans. (1990) 3161.
[9] E.W. Abel, K.G. Orrell, A.G. Osborne, H.M. Pain, V. Šik, M.B. Hursthouse, K.M.A. Malik, J. Chem. Soc. Dalton Trans. (1994) 3441.
[10] E.W. Abel, E.S. Blackwall, P.J. Heard, et al., J. Chem. Soc. Dalton Trans. (1994) 445.
[11] E.W. Abel, P.J. Heard, K.G. Orrell, M.B. Hursthouse, K.M.A. Malik, Polyhedron 13 (1994) 2501.

[12] E.W. Abel, T.P.J. Coston, K.G. Orrell, V. Šik, D. Stephenson, J. Magn. Reson. 70 (1986) 34.
[13] E.W. Abel, S.K. Bhargava, K.G. Orrell, Prog. Inorg. Chem. 32 (1984) 1.
[14] R. Knorr, J. Ruhdorfer, J. Mehlstäubl, P. Böhrer, D.S. Stephenson, Chem. Ber. 126 (1993) 747.
[15] D.S. Stephenson, G. Binsch, DNMR 5, Program 365, Quantum Chemistry Program Exchange, Indiana University, USA, 1978.
[16] J.C. Baldwin, W.C. Kaska, Inorg. Chem. 14 (1975) 2020.
[17] D.H. Goldsworthy, Ph.D. Thesis, University of Exeter, 1980.
[18] A.J. Blake, A.J. Lavery, T.J. Hyde, M. Schroder, J. Chem. Soc. Dalton Trans. (1989) 965.
[19] D.F. Shriver, Manipulation of Air-Sensitive Compounds, McGraw-Hill, New York, 1969.
[20] J.A. Darr, S.R. Drake, M.B. Hursthouse, K.M.A. Malik, Inorg. Chem. 32 (1993) 5704.
[21] N.P.C. Walker, D. Stuart, Acta Crystallogr. A39 (1983) 158.
[22] G.M. Sheldrick, Acta Crystallogr. A46 (1990) 467.
[23] G.M. Sheldrick, SHELXL-93 Program for Crystal Structure Refinement, University of Gottingen, Germany, 1993.